



# Mid Infrared Tomography of Polymer Pipes

D. A. Hutchins<sup>1</sup> · P. Huthwaite<sup>2</sup> · L. A. J. Davis<sup>1</sup> · D. R. Billson<sup>1</sup> · L. Senni<sup>3</sup> · S. Laureti<sup>4</sup> · M. Ricci<sup>4</sup>

Received: 25 September 2019 / Accepted: 28 August 2020 / Published online: 14 September 2020  
© The Author(s) 2020

## Abstract

Mid-infrared signals in the 2–5  $\mu\text{m}$  wavelength range have been transmitted through samples of polymer pipes, as commonly used in the water supply industry. It is shown that simple through-transmission images can be obtained using a broad spectrum source and a suitable camera. This leads to the possibility of tomography, where images are obtained as the measurement system is rotated with respect to the axis of the pipe. The unusual 3D geometry created by a source of finite size and the imaging plane of a camera, plus the fact that refraction at the pipe wall would cause significant ray bending, meant that the reconstruction of tomographic images had to be considered with some care. A result is shown for a thinning defect on the inner wall of a polymer water pipe, demonstrating that such changes can be reconstructed successfully.

**Keywords** Tomography · Mid infrared

## 1 Introduction

Infrared signals have been used for some time for industrial measurements. One example is infrared spectroscopy [1], which can be used for the characterisation of materials, especially food [2]. Typically, the technique relies on the absorption of signals in the 0.78–2  $\mu\text{m}$  wavelength range. In general, the resultant spectra are complex, being due to vibrational modes and overtones of the main absorption bands. However, it is still possible to identify the presence of constituents and their concentration, often via the use of chemometrics [3]. In this near infrared (NIR) wavelength range, signals will penetrate into many non-conducting mate-

rials, often to a limited extent due to absorption and scattering mechanisms. This is made use of in certain medical procedures, where there is reasonable transmission of NIR signals through human tissue. This allows techniques such as blood oxygen measurement by differential absorption at two wavelengths [4] and breast imaging for cancer diagnosis [5] to be developed. Other applications include intraocular imaging where there is greater penetration into the eye than in the visible region [6, 7].

NIR signals generated over a range of discrete wavelengths (e.g. using laser diodes) have also received attention for the detection of contaminants in food by direct imaging [8], where differential absorption as a function of wavelength can provide images of changes in structure. This again makes use of the fact that major absorption bands exist in many materials in the NIR region, and the fact that laser diode sources are available at specific wavelengths. When used over a range of wavelengths, including both NIR and mid-IR signals (the latter being sometimes defined as being signals at wavelengths of up to approximately 5  $\mu\text{m}$ ), the technique is often referred to as hyperspectral imaging, where again monitoring of food quality is a major application area [9–11]. Note that discrete NIR wavelengths can also be used to detect changes in other materials such as polymers, composites and foams [12]. Tomographic techniques have also been attempted using NIR signals, in particular for medical imaging [13–15]. The predominance of diffuse scattering makes attenuation and the detection of usable signals more

**Electronic supplementary material** The online version of this article (<https://doi.org/10.1007/s10921-020-00714-0>) contains supplementary material, which is available to authorized users.

✉ D. A. Hutchins  
d.a.hutchins@warwick.ac.uk

- <sup>1</sup> School of Engineering, University of Warwick, Coventry CV4 7AL, UK
- <sup>2</sup> Department of Mechanical Engineering, Imperial College London, South Kensington Campus, London SW7 2AZ, UK
- <sup>3</sup> Dipartimento di Ingegneria, Polo Scientifico Didattico di Terni, Università di Perugia, Strada di Pentima 4, 05100 Terni, Italy
- <sup>4</sup> Dipartimento di Ingegneria Informatica, Modellistica, Elettronica e Sistemistica, Università della Calabria, Via Pietro Bucci, Arcavacata, 87036 Rende, CS, Italy

difficult, but models are being investigated to enable diffuse scattering tomography to be implemented [16].

In some situations, excessive attenuation and scattering in the NIR region can limit applications in the imaging of engineering materials such as polymers. This is the case the polymers used by utilities companies for the supply of water and gas. There is a need to inspect this pipework, not only for defects in manufacture, but also for degradation during use and the inspection of fusion joints between pipe sections. There are a range of materials used for such pipework, with one common material being high-density polyethylene (HDPE). These are colour-coded within the EU for practical use—blue for water, yellow for gas and black for sewage/drainage. Some work has been reported in larger pipes (220–450 mm outer diameter) where ultrasonic phased arrays were used to detect defects in the form of flat-bottomed holes [17]. Microwave technologies have also been described for evaluating electrofusion welds [18]. Images of changes in dielectric properties of polymer pipework can be measured using electrical capacitance tomography over a limited region [19], but needs careful use in terms of distance from the sample. X-ray CT has also been investigated for measuring the physical state of polymers, and could be applied to pipe inspection [20]. However, a technique that did not rely on ionizing radiation would be of benefit for routine inspection, for example when the pipework is being laid, as the adverse health and safety aspects of X-rays would be mitigated.

Despite its advantages, little has been reported on the use of mid-IR signals in the 2–5  $\mu\text{m}$  region for pipework inspection. This is despite the fact that the addition of dyes is a challenge for penetration of NIR signals in such polymers, in that primary absorption bands in the visible have fractional frequencies in the NIR region, and this makes measurements in this wavelength region difficult. Extension into the mid-IR at wavelengths  $>2 \mu\text{m}$  in principle allows greater penetration, due to the fact that interaction with visible dyes is often much reduced. The availability of hyperspectral cameras over the mid-IR wavelength range makes the measurements convenient, when used with a broad spectrum halogen or wire filament source, but the inspection of pipework in this way does not seem to have been reported. Contrast to defects within a pipe would be expected from both scattering and refraction effects, and thus any imaging system would need to be developed so as to deal with these, and hence find defects such as wall thinning. In this paper, it is shown that such mid-IR signals can be used for tomographic reconstruction of cross-sections through HDPE pipes, and that an artificial defect can be located by this means.

## 2 Apparatus and Experiment

The experiments were conducted using a NIR through-transmission imaging system. Figure 1 shows a diagram of the apparatus used in the mid-IR measurement. The water pipe was a blue HDPE sample with an inner diameter of  $25 \pm 1 \text{ mm}$  and an outer diameter of  $32 \pm 1 \text{ mm}$ , wall thickness  $3.4 \pm 0.2 \text{ mm}$ . It was mounted vertically on a motorised rotation stage, so that tomographic data could be recorded at pre-determined angular intervals (in this case  $5^\circ$ ). The mid-IR source was a 12 V, 20 W halogen filament bulb of 10 mm diameter (Micropack HL-2000 from Ocean Optics, Inc., USA) with fibre-optic coupling to lenses if required. No collimation was used. The output wavelength range was 2–5  $\mu\text{m}$ . The beam angle ( $\theta$ ) in the horizontal plane was controlled using an aperture as shown (noting that the pipe was positioned vertically). This minimised leakage of light around the outside of the pipe, which could otherwise dominate the received signal.

The transmitted light intensity was then captured at the image plane using a FLIR SC7000 video camera (FLIR Systems, Inc., USA). This had a pixel resolution of  $640 \times 512$  with a 15  $\mu\text{m}$  pixel pitch, and operated over a 1.5–5.1  $\mu\text{m}$  wavelength range with noise levels as low as 20 mK. The lens allows efficient collection of mid-IR energy over the angular range ( $\theta$ ) which is then focussed onto the detector for increased sensitivity. The camera was fitted with a filter that removed light energy at wavelengths below 2  $\mu\text{m}$ . A chopper wheel modulated the mid-IR energy at frequencies in the range 50–100 Hz, the modulation frequency being dictated by the rotation speed of the chopper wheel (100 Hz being the maximum frame rate of the camera). This arrangement allowed image frames to be recorded both in the presence and absence of illumination. After averaging successive frames in each of the two states (illumination on or off), an image representing the difference between the on and off states was obtained, effectively correcting for any stray light present in the room containing the experiment or black-body radiation from the sample. The camera focus was adjusted so as to collect the through-transmitted mid-IR signal as efficiently as possible. Images were then recorded at  $5^\circ$  intervals of  $\gamma$  as the sample was rotated manually. Note that an automated scan would be possible in an industrial setting.

The pipe itself, being an example of that used in real applications, was not perfectly straight. This became obvious during rotation, and was observed in the data taken by the camera. A photograph of the pipe is shown in Fig. 2, where the half-thickness defect in the form of a flat-bottomed cylindrical hole of diameter 5 mm and depth 4 mm is visible. Note also the non-ideal scratched surface condition of the pipe inner wall.

Examples of the raw mid-IR images obtained from the camera with the pipe rotated at  $10^\circ$  angular intervals are

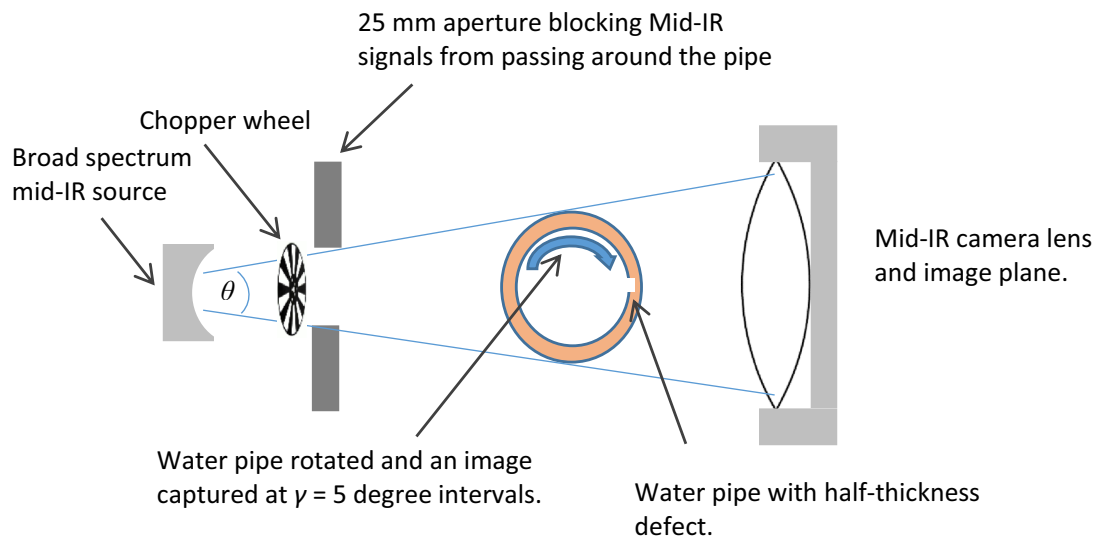


**Fig. 1** Plan view of the experiment to collect mid-IR tomographic data after transmission through a blue HDPE pipe (Color figure online)

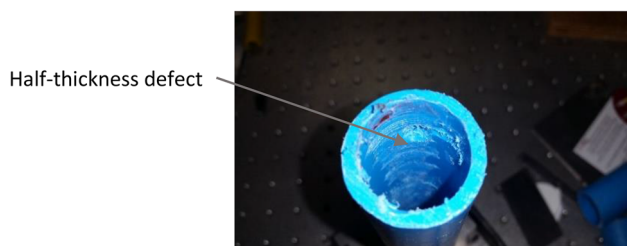


**Fig. 2** Photograph of the HDPE pipe containing the artificial defect in the form of a flat-bottomed hole

shown in Fig. 3. In each case, the defect appears towards the top of the image as a darker circular area, with a brighter inner core. This is thought to be due to the edges of the hole causing refraction and reflection of through-transmitted mid-IR radiation, with a small central brighter region due to a smaller wall thickness at that location. Note the light leakage around the object on the right hand side of each image, and

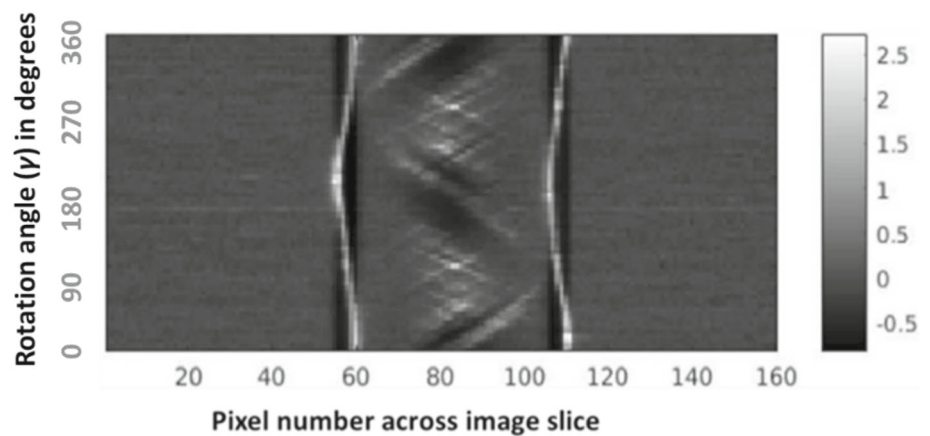
**Fig. 3** Images taken with the apparatus of Fig. 1, cropped to remove some of the light that had diffracted around the outer pipe wall. The images are at  $10^\circ$  intervals, with the sample rotated clockwise from left to right



the presence of a faint brighter region along a central vertical axis, where refraction of mid-IR energy would be the least. Note that there is significant noise, visible by the graininess in each image, due to the low level of optical transmission. The hope was that tomographic reconstruction would help to identify the presence of the hole more clearly.

To get an idea of the type of data that could be used for input into a tomographic reconstruction algorithm, Fig. 4 shows a representation formed from a set of horizontal slices, taken from each image as the pipe was rotated, and stacked vertically. These slices were all located at the same horizontal plane containing the defect. The angle of rotation at which each image was recorded is along the vertical axis, and the image slices stretch across the image at each angle. It is evident from this image that the external wall of the pipe, seen as the lighter outline caused by light diffraction around the outer wall, moved side to side as the pipe was rotated. Also evident is an oscillating feature with an almost sinu-

**Fig. 4** Representation of a set of horizontal image slices, taken along the same horizontal section through the pipe, as the pipe was rotated at discrete rotation angles ( $\gamma$ ). The image amplitude scale is arbitrary, chosen to highlight the main features of the signal



soidal path—this is the track of the defect as the pipe was rotated. It shows up as a lighter path because of increased mid-IR transmission through the pipe wall at that point, and is surrounded either side by a darker region as noted in the images of Fig. 3. As the pipe is rotated, the defect oscillates between the central alignment axis of the mid-IR beam and the two extremities of the pipe wall, as would be expected from geometrical considerations.

### 3 Tomographic Reconstruction

#### 3.1 Initial Reconstructions

Having shown that data suitable in principle for tomographic reconstruction could be obtained, the problem now was to find a suitable algorithm to do this. Tomographic reconstructions are effectively inversion problems, attempting to produce an image which matches the measured data. There are two key elements to any such algorithm: the forward model, which estimates what the measured data would be for a particular image and the inversion approach, which aims to determine which image will produce the right data under the specific forward model. Also linked to these are regularisation schemes which introduce additional information to steer the image towards a particular solution, which can be vital when the measured data contains errors, noise, or is under-sampled in some way.

For a truly accurate forward model in this scenario, it would be necessary to fully model the IR wave behaviour, including diffraction, reflection, attenuation and refraction as it passes through the pipe. In theory this would correspondingly produce the most accurate results; within geophysics this has been demonstrated in full wave inversion [21] and in guided wave tomography it has also been shown that accurately accounting for scattering behaviour gives the most accurate results [22]. However, this is likely to be very slow, challenging to invert and potentially very sensitive to errors

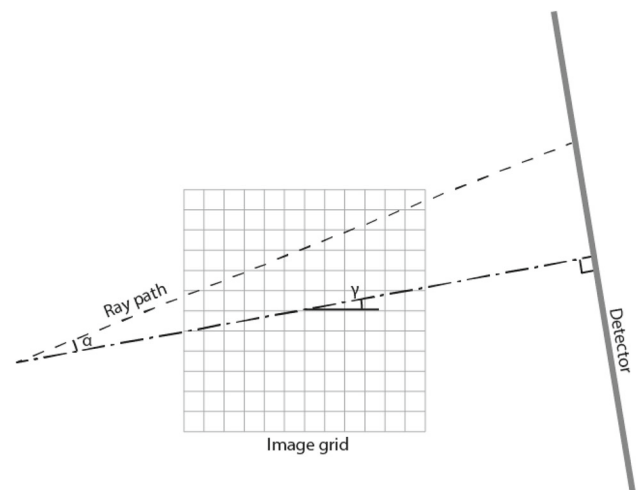


**Fig. 5** Configuration of the imaging plane for a standard reconstruction

and noise. Therefore consideration is restricted to the asymptotic high-frequency approximation, i.e. the ray theory of geometrical optics. This is taken further by neglecting refraction too, i.e. assuming straight rays, which greatly simplifies the inversion. This can be expressed as

$$p(\gamma, \alpha) = \int_{ray} f[\mathbf{r}(\gamma, \alpha, s)] ds, \quad (1)$$

where  $p(\gamma, \alpha)$  is the projection data, for a projection angle of  $\gamma$  and a relative angle of  $\alpha$  respectively. Also,  $f(\mathbf{r})$  is the field data (typically attenuation for radiographic CT and reconstructing amplitude projections, or slowness—the reciprocal of wave velocity—when imaging arrival time values) at position  $\mathbf{r}$  in space. The specific value for  $\mathbf{r} = \mathbf{r}(\gamma, \alpha, s)$  is determined via geometry, as defined by the combination of the two angles and the position  $s$  along the path. Figure 5 illustrates this, showing both the angles referred to above and the imaging grid.

The straight ray assumption is relied upon within radiographic CT, and the algorithms from this area can therefore



be used for this problem. One of the most common is the filtered back-projection approach [23]. In this algorithm the Fourier slice theorem is invoked, which states that the 1D Fourier transform of a single projection line at one angle  $\gamma$  corresponds to a slice through the 2D Fourier transform of the full map  $f$  at the same angle. Each projection can be back-projected (smeared) across the image space, reconstructing an image, but this leaves certain frequency components amplified because the Fourier space is not evenly covered by the slices. Therefore, a filter is applied to each projection prior to projecting to correct for this. The resulting filtered back-projection algorithm (and variations on it) is used in almost all commercially available CT systems.

Iterative algorithms are an alternative. These have the advantage that they work well with arbitrary sampling including subsampling, as well as providing straightforward methods of incorporating regularisation. However, these algorithms are typically slow. There are a number of different algorithms (e.g. algebraic reconstruction technique—ART [24], simultaneous iterative reconstruction technique—SIRT [25]), but essentially the principle is to simulate rays through the current reconstruction, compare the resulting values to the measured values, then correct by projecting any residual along the corresponding ray paths.

Taking the slices displayed in Fig. 4, it is possible to reconstruct an initial image of the cylinder generated using the ART algorithm. This is shown in Fig. 6. It would be expected that the sample would exhibit a high degree of self-focussing in the direction of the detector, due to refraction effects at the sample walls. However, it should be noted that this is a reconstruction of effective attenuation; the scattering and refraction is neglected and the quantity produced is a value corresponding to the local change in amplitude. It is evident from the reconstructed image that the defect has been detected, but that the contrast is not high and the resolution is not good enough. Ray-based methods have been shown to give significantly lower resolution compared to methods which account for diffraction [26, 27]. Further, there are various artefacts that are present, in addition to the area where the defect is located, and the pipe walls are a prominent feature. There are several reasons for the presence of artefacts and a reduction in resolution. One is the effect of the pipe walls—refraction will occur due to the large difference in wave speed between the polymer and the surrounding air, and there is a high intensity of light beyond the outer wall due to direct transmission from the source and around the object. In addition, due to the geometry, the fan beam angle  $\theta$  is restricted due to the need to exclude light beyond the outer wall boundary. It can also be seen from Fig. 4 that the feature representing the defect location is less distinct when it is at an angle where it is masked by the finite wall thickness (effectively at the edge of the fan beam angular range). Note that while techniques such as refractive index matching

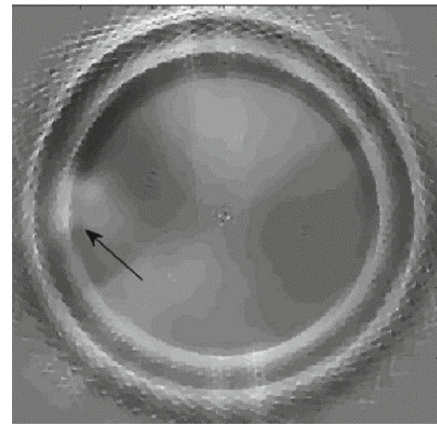


**Fig. 6** An initial reconstruction of the HDPE pipe from mid-IR data at the horizontal section containing the defect

via coatings could be used to reduce such effects, this is not practical for industrial utility piping.

This variation in intensity effectively limits the range of angles available for the reconstruction: where the beam is too weak to be received by the camera, this data cannot be used in the reconstruction. The effect of the limited range of data available for reconstruction can be illustrated by some simulations, whereby the characteristics and experimental data and that which could be obtained in a perfect measurement are compared, as in Fig. 7. In the presence of a full data set for a perfect case, Fig. 7a, the uniform track of the defect path leads to good tomographic reconstruction of an image of the defect. If data is simulated so as to be closer to that seen experimentally, Fig. 7b, the image of the defect is degraded and artefacts are present due to angular under-sampling effects. Thus, a more sophisticated imaging technique was required.

### 3.2 A More Sophisticated Reconstruction Algorithm

As highlighted previously, several assumptions are made in the reconstruction approach which appear to significantly affect the accuracy of the result. There is a lot of uncertainty in the refraction behaviour (in particular) which causes issues; because the physics does not match the modelled scenario, the problem effectively becomes heavily underdetermined.

In the initial approach, a full 2D image of the cross section was considered, where the challenge was to determine the attenuation at every point in the grid. However, it is recognised that the pipe itself only occupies a narrow range of this grid, and therefore the problem can be reformulated, to just consider pixels within the pipe wall. It is also recognised that determining whether the defect is at the inner or outer surface is not of huge benefit, so the thickness of the pipe wall is actually neglected and can be treated as a thin-walled pipe of one-pixel width, as illustrated in Fig. 8. By having fewer pixels, there is a reduction in parameters to be inverted, reduc-

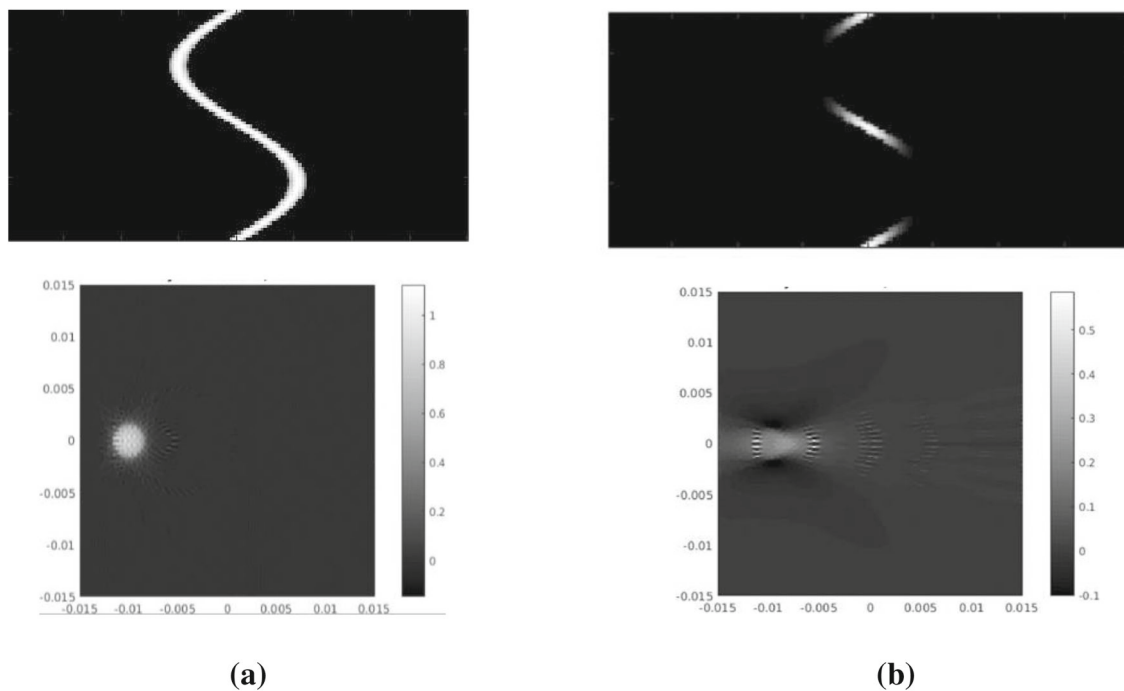


**Fig. 7** Simulations of the performance of initial reconstructions, using the data shown in Fig. 4. **a** Simulated full data at high contrast, and **b** partial data to simulate the effective masking of the defect by the pipe wall when at certain rotation angles

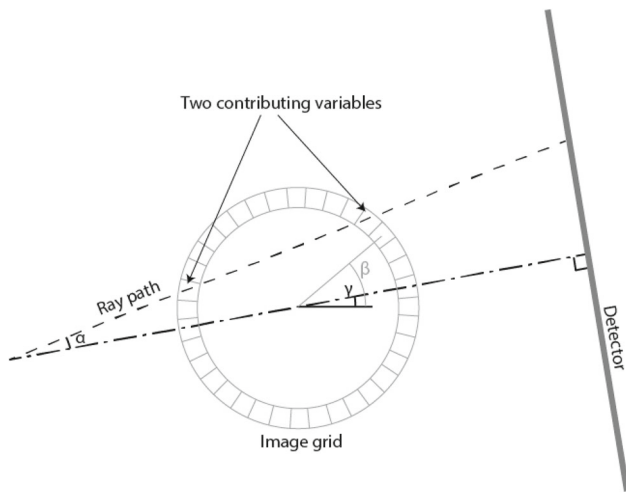


**Fig. 8** Imaging form with a single line of pixels around the thin-walled pipe circumference

ing the underdetermined nature of the problem and helping with the inversion. This can be considered a regularisation approach, since it effectively steers the inversion towards a particular solution based on prior/external information.

As highlighted in Fig. 8, there are now two pixel values/variables in the straight-ray model which contribute to the values measured at each detector position, where the ray enters and exits the pipe. Under this model

$$p(\gamma, \alpha) = f'[\beta(\gamma, \alpha)_{entry}] + f'[\beta(\gamma, \alpha)_{exit}], \quad (2)$$

where now,  $f'$  is the 1D function representing the field around the circumference, as a function of the angle  $\beta$ . Determining  $\beta$  for a particular pair of  $\alpha$  and  $\gamma$  is straightforward by geometric considerations.

At this point, it is possible to perform an inversion in much the same way as on a standard grid; the flexibility of iterative methods e.g. ART are likely to be preferable for this. However, it is noted that given that just two variables affect any resulting point in the projected data, there is likely to be limited interdependence compared to the full grid-based imaging. Therefore it is proposed to just use a single back-projection iteration to generate an image

$$f'(\beta) = \int p[\gamma, \alpha(\gamma, \beta)]d\gamma, \quad (3)$$

where now  $\alpha(\gamma, \beta)$  needs to be calculated for each pair of  $\gamma$  and  $\beta$ . Physically, this projects the measured values onto the circle corresponding to the pipe wall and repeats this for each projection, summing each time (integrating in the continuous case). This approach will include some errors in the reconstruction: effectively any features on the far side of the pipe will be smeared across the near side and vice versa, however it is hoped that this will not cause major issues. By summing across the multiple projections these components should be minimised.

It was necessary as a first step to remove unwanted data, such as that arising from mid-IR signals going around the external wall of the pipe. This enhances the dynamic range for

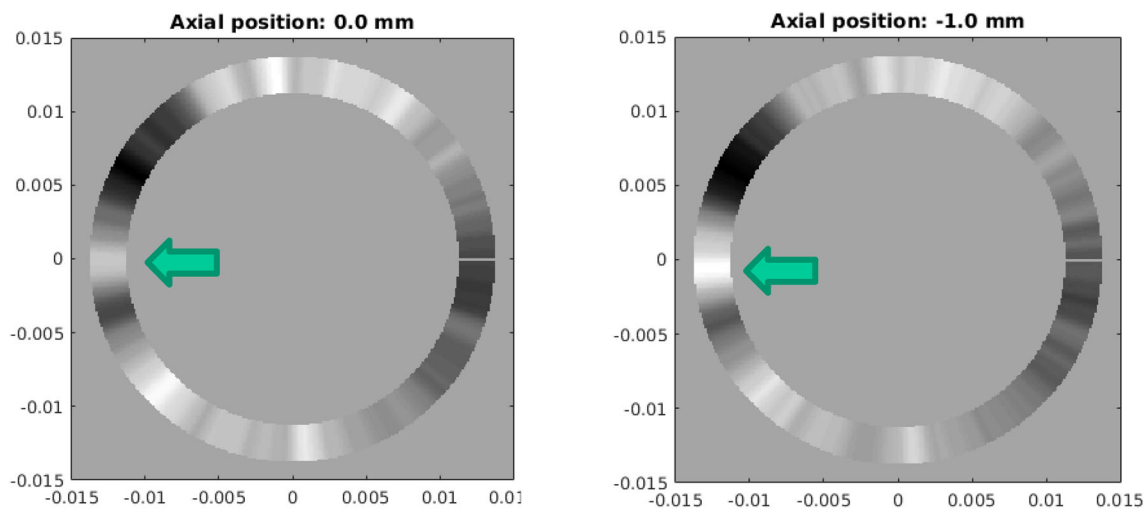
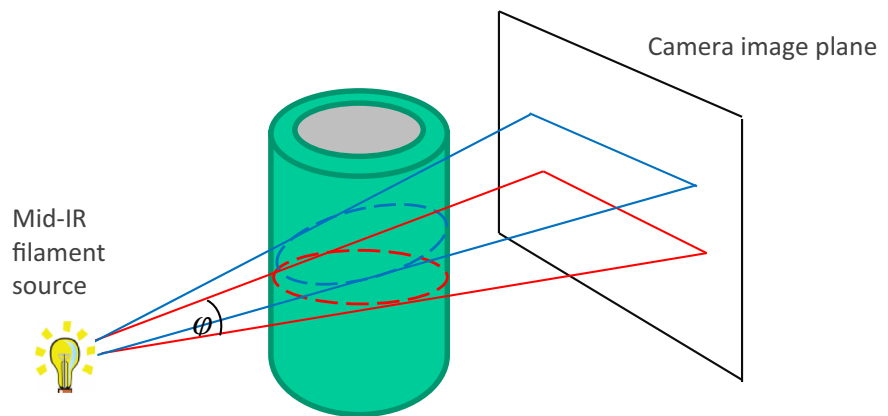


**Fig. 9** Reconstructions at two axial locations. Units for both images are (m) for both axes (i.e. plots represent 15 mm × 15 mm)

**Fig. 10** Schematic representation of the geometry that needed to be considered for a more appropriate tomographic reconstruction scheme



the region of interest, and hence should improve image quality. The effective regularisation helps to mitigate the removal of data like this. Specifically, in an inversion of the Beer-Lambert relationship, we calculated

$$p = \ln \frac{I}{I_0}, \quad (4)$$

where  $I$  is the measured intensity and  $I_0$  is a baseline reference; this matches the standard CT approach. We did not have a baseline, so we took an average of all the projections, which, since the defect is relatively small, will be a good approximation to a projection through a defect-free pipe. The reconstruction of the defect will therefore be relative to the undamaged pipe. In addition, the values of any measurement more than 20 mm from the centre of the beam was set to 0, since, as shown in Fig. 4, these components do not contain meaningful information and are primarily noise. From Fig. 4 this removed the components less than 70 pixels or greater than 100 pixels. This data was then passed to the projection algorithm.

The output from this is a 1D function around the circumference at a single axial location of the pipe. Two example reconstructions from this are shown in Fig. 9, at two different locations. All these circumferential images in this paper have 600 pixels around the circumference. The green arrow marks the expected location of the defect. It can be seen that at the axial location away from the defect (at 0.0 mm), the indication of the flat-bottomed hole is weak, whereas at a position of  $-1.0$  mm there is a much clearer indication. In practice, it is possible to identify the presence of the defect with prior knowledge that it is present and its location; the major background variations which can be seen in both reconstructions would make it highly challenging to identify such defects in practice. However, the low computational overhead of this approach does enable more information to be provided to the viewer by combining the data from a range of axial locations.

It should be noted that when reconstructing different axial slices, it is necessary to consider the full 3D nature of the problem. The geometrical setup is illustrated in Fig. 10. This illustrates the fact that the camera, fitted with a lens, collected data over a 3-dimensional volume. The angle  $\theta$  (see Fig. 1)

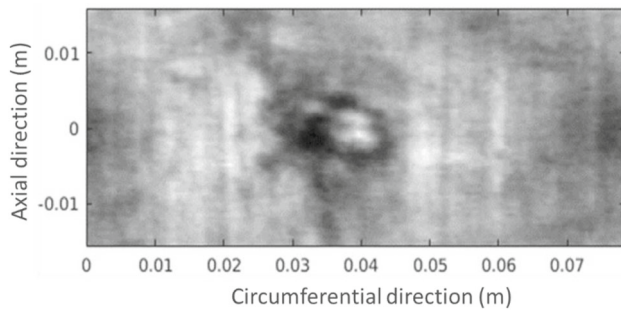


**Fig. 11** Full reconstruction of flat-bottomed hole defect from mid-IR data

was restricted by an aperture to a certain range in the horizontal direction, but the camera collected data over a set of paths such as that shown in blue in Fig. 9 at various angles ( $\varphi$ ) to the horizontal axis, whose range was dictated by the camera lens. The problem then became one of accounting for the elevation angle in the reconstruction in addition to the in-plane angles; again the geometric considerations made it straightforward to achieve this.

The result of this treatment is shown in Fig. 11. It can be seen that the flat-bottomed hole has been reconstructed successfully in the expected form—a brighter centre surrounded by a ring of lower transmitted intensity. This arises from refraction at the defect edges, causing a darker area around the flat region of the centre of the hole.

Producing the reconstruction in this form has a clear significant benefit. The defect can be clearly distinguished from the variations in the pipe wall itself, which was not possible by just looking at a single cross section of the pipe. There is very little evidence of the smearing of features on the opposite surfaces, which indicates that the approach is fairly robust to these errors. There is a slight darkening around 0.0 m in the axial direction and 0.0 m and 0.08 m in the circumferential directions, which is likely to correspond to the defect projected onto the opposite surface, but this does not interfere with our ability to identify the defect.

It is possible to see a darker ring around the lighter coloured defect, in consistency with the original images (Fig. 3). This is because the method is not correcting for the refraction and diffraction effects which occur when the wave passes through the pipe wall. Rather than being a reconstruction of material attenuation, the image should be interpreted as being a map of the total energy received along that ray path, which can include attenuation affects themselves, but also aspects such as refractive focusing/defocusing of the wavefield.

There is also the potential for some geometric unsharpness in the reconstruction, caused by the source not being a true point source. The bulb diameter of 10 mm is likely to

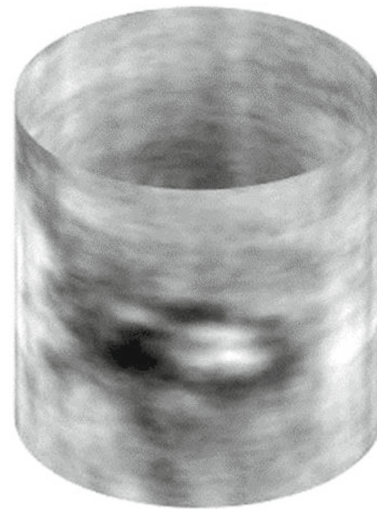


**Fig. 12** Reconstruction shown in cylindrical format (see Visualisation 1 for a rotated view of the reconstruction)

contribute blurriness in the reconstruction, in addition to the other approximations.

Note that this method of reconstruction also lends itself to a 3D display of the data along the length of the pipe, as shown in Fig. 12, and available within the Supplementary Material as a video as Fig. 13.

## 4 Conclusions

It has been demonstrated that mid-IR signals can be used to collect through-transmission data for HDPE pipes, and that this is able to detect the presence of defects. With careful consideration of the geometrical complexities, it was possible to develop a tomographic reconstruction scheme that could consider the use of a mid-IR camera, fitted with a lens, together with a broad bandwidth source operating over a wide angular range. It is thought that this technique would be of interest where the internal structure of polymer pipework needed to be determined. The technique could be improved further by using brighter sources of mid-IR signals, and a more automated scanning system.

**Acknowledgements** This work was supported by the UK Engineering and Physical Sciences Research Council (EPSRC), Grant Number EP/L022125/1, through the UK Research Centre in NDE (RCNDE). One of the authors (PH) is also funded under an EPSRC Fellowship (EP/M020207/1).

**Open Access** This article is licensed under a Creative Commons Attribution 4.0 International License, which permits use, sharing, adaptation, distribution and reproduction in any medium or format, as long as you give appropriate credit to the original author(s) and the source, provide a link to the Creative Commons licence, and indicate if changes were made. The images or other third party material in this article are included in the article's Creative Commons licence,



unless indicated otherwise in a credit line to the material. If material is not included in the article's Creative Commons licence and your intended use is not permitted by statutory regulation or exceeds the permitted use, you will need to obtain permission directly from the copyright holder. To view a copy of this licence, visit <http://creativecommons.org/licenses/by/4.0/>.

## References

- Salzer, R., Siisler, H.W. (eds.): *Infrared and Raman Spectroscopic Imaging*. Wiley-VCH Verlag GmbH and Co., Weinheim (2009)
- Sun, D.-W.: *Infrared Spectroscopy for Food Quality Analysis and Control*. Academic, New York (2009)
- Osbourne, B.G.: Near-infrared spectroscopy in food analysis. In *Encyclopedia of Analytical Chemistry*. Wiley, Chichester (2006)
- Myers, D., McGraw, M., George, M., Mulier, K., Beilman, G.: Tissue hemoglobin index: a non-invasive optical measure of total tissue haemoglobin. *Crit. Care* **13**(Suppl 5), S2 (2009)
- El-Sharkawy, Y.H., El-Sherif, A.F.: High-performance near-infrared imaging for breast cancer detection. *J. Biomed. Opt.* **19**, 16018 (2014)
- Krohn, J., Ulltang, E., Kjersem, B.: Near-infrared transillumination photography of intraocular tumours. *Br. J. Ophthalmol.* **97**, 303574 (2013)
- Yusuf, I.H., Peirson, S.N., Patel, C.K.: Occlusive IOLs for intractable diplopia demonstrate a novel near-infrared window of transmission for SLO/OCT imaging and clinical assessment. *Investig. Ophthalmol. Vis. Sci.* **52**(6), 3737–3743 (2011)
- Pallav, P., Diamond, G.G., Hutchins, D.A., Green, R.J., Gan, T.H.: A near infrared (NIR) technique for imaging food materials. *J. Food Sci.* **74**(1), E23–E33 (2009)
- El-Masry, G., Sun, D.-W., Allen, P.: Near-infrared hyperspectral imaging for predicting colour, pH and tenderness of fresh beef. *J. Food Eng.* **110**(1), 127–140 (2012)
- Gowen, A., O'Donnell, C.P., Cullen, P.J., Downey, G., Frias, J.M.: Hyperspectral imaging—an emerging process analytical tool for food quality and safety control. *Trends Food Sci. Technol.* **18**(12), 590–598 (2007)
- Wang, W., Paliwal, J.: Near-infrared spectroscopy and imaging in food quality and safety. *Sens. Instrum. Food Qual. Saf.* **1**(4), 193–207 (2007)
- Pallav, P., Diamond, G.G., Hutchins, D.A., Gan, T.H.: A near infrared technique for nondestructive evaluation. *Insight* **50**(5), 244–248 (2008)
- McBride, T.O., Pogue, B.W., Jiang, S., Österberg, U.L., Paulsen, K.D.: A parallel-detection frequency-domain near-infrared tomography system for hemoglobin imaging of the breast in vivo. *Rev. Sci. Instrum.* **72**, 1817 (2001)
- Dehghani, H., Eames, M.E., Yalavarthy, P.K., Davis, S.C., Srinivasan, S., Carpenter, C.M., Pogue, B.W., Paulsen, K.D.: Near infrared optical tomography using NIRFAST: algorithm for numerical model and image reconstruction. *Numer. Methods Biomed. Eng.* **25**(6), 711–732 (2009)
- Dehghani, H., Pogue, B.W., Poplack, S.P., Paulsen, K.D.: Multiwavelength three-dimensional near-infrared tomography of the breast: initial simulation, phantom, and clinical results. *Appl. Opt.* **42**(1), 135–145 (2003)
- Hoshi, Y., Yamada, Y.: Overview of diffuse optical tomography and its clinical applications. *J. Biomed. Opt.* **21**, 091312 (2016)
- Hagglund, F., Robson, M., Troughton, M.J., Spicer, W., Pinson, I.R.: A novel phased array ultrasonic testing (PAUT) system for on-site inspection of welded joints in plastic pipes. In: Presented at 11th European Conference on Non-destructive Testing (ECNDT) (2014)
- Murphy, K., Lowe, D.: Evaluation of a novel microwave based NDT inspection method for polyethylene joints. In: Proceedings of the ASME 2011 Pressure Vessels and Piping Conference (ASME, 2011), Paper No. PVP2011-58086, pp. 321–327
- Al Hosani, E., Zhang, M., Soleimani, M.: A limited region electrical capacitance tomography for detection of deposits in pipelines. *IEEE Sens. J.* **15**(11), 6089–6099 (2015)
- Warnett, J.M., Titarenko, V., Kiraci, E., Attridge, A., Lionheart, W.R.B., Withers, P.J., Williams, M.A.: Towards in-process X-ray CT for dimensional metrology. *Meas. Sci. Technol.* **27**, 035401 (2016)
- Pratt, R.G.: Seismic waveform inversion in the frequency domain, Part 1: theory and verification in a physical scale model. *Geophysics* **64**(3), 888–901 (1999)
- Huthwaite, P.: Guided wave tomography with an improved scattering model. *Proc. R. Soc.* **A472**, 20160643 (2016)
- Kak, A.C., Slaney, M.: *Principles of Computerized Tomographic Imaging*. IEEE, New York (1988)
- Gordon, R., Bender, R., Herman, G.T.: Algebraic reconstruction techniques (ART) for three-dimensional electron microscopy and X-ray photography. *J. Theor. Biol.* **29**(3), 471–481 (1970)
- Gilbert, P.: Iterative methods for the three-dimensional reconstruction of an object from projections. *J. Theor. Biol.* **36**(1), 105–117 (1972)
- Williamson, P.R.: A guide to the limits of resolution imposed by scattering in ray tomography. *Geophysics* **56**(2), 202–207 (1991)
- Huthwaite, P., Simonetti, F.: High-resolution imaging without iteration: a fast and robust method for breast ultrasound tomography. *J. Acoust. Soc. Am.* **130**(3), 1721–1734 (2011)

**Publisher's Note** Springer Nature remains neutral with regard to jurisdictional claims in published maps and institutional affiliations.